

Three-Dimensional Subzone-Based Reconstruction Algorithm for MR Elastography

Elijah E.W. Van Houten,^{1*} Michael I. Miga,¹ John B. Weaver,² Francis E. Kennedy,¹ and Keith D. Paulsen^{1,3}

Accurate characterization of harmonic tissue motion for realistic tissue geometries and property distributions requires knowledge of the full three-dimensional displacement field because of the asymmetric nature of both the boundaries of the tissue domain and the location of internal mechanical heterogeneities. The implications of this for magnetic resonance elastography (MRE) are twofold. First, for MRE methods which require the measurement of a harmonic displacement field within the tissue region of interest, the presence of 3D motion effects reduces or eliminates the possibility that simpler, lower-dimensional motion field images will capture the true dynamics of the entire stimulated tissue. Second, MRE techniques that exploit model-based elastic property reconstruction methods will not be able to accurately match the observed displacements unless they are capable of accounting for 3D motion effects. These two factors are of key importance for MRE techniques based on linear elasticity models to reconstruct mechanical tissue property distributions in biological samples. This article demonstrates that 3D motion effects are present even in regular, symmetric phantom geometries and presents the development of a 3D reconstruction algorithm capable of discerning elastic property distributions in the presence of such effects. The algorithm allows for the accurate determination of tissue mechanical properties at resolutions equal to that of the MR displacement image in complex, asymmetric biological tissue geometries. Simulation studies in a realistic 3D breast geometry indicate that the process can accurately detect 1-cm diameter hard inclusions with 2.5× elasticity contrast to the surrounding tissue. Magn Reson Med 45:827–837, 2001. © 2001 Wiley-Liss, Inc.

Key words: MR elastography; elasticity reconstruction; regularized inversion techniques; three-dimensional tissue mechanics

The basic objective of the emerging field of MR elastography (MRE) is the realization of an imaging technique which provides quantitative assessment of the in vivo mechanical properties of tissue. As of yet, no direct correlation has been found between mechanical property contrast and a molecular contrast immediately discernible through standard MR imaging sequences. This necessitates the development of indirect imaging processes, most commonly algorithms which operate on the displacement or strain images that can be detected directly through MR phenomenon (1–14). The reconstructive nature of these methods renders them sensitive to the accuracy with

which they can account for behavior observed in the imaged data; that is, the final elastographic image produced by such indirect imaging algorithms can only be as good as the fundamental assumptions which underlie the reconstruction approach.

One of the simplest relationships between displacement behavior and elastic property values within a material is found in the theory of linear, isotropic elasticity (15). Through Hooke's Law, which assumes a linear relation between the imposed stresses on a body and its resulting strains, and the conditions of dynamic equilibrium, a conditional relationship can be developed between a continuum's displacement field and its mechanical property distribution. When expressed in partial differential equation (PDE) form this correlation is known as Navier's equation:

$$\nabla \cdot G \nabla \mathbf{u} + \nabla(\lambda + G) \nabla \cdot \mathbf{u} = \rho \frac{\partial^2 \mathbf{u}}{\partial t^2}, \quad [1]$$

where \mathbf{u} is the displacement vector, G and λ are Lamé's constants describing the stiffness and mechanical behavior of the medium, and ρ is the material density. Young's modulus of elasticity is related to Lamé's constants through the expressions $G = [E/2(1+\nu)]$ and $\lambda = [\nu E/(1+\nu)(1-2\nu)]$ with Poisson's ratio ν .

In the case of large deformations, biological tissue does not typically exhibit linear behavior. However, small levels of strain within tissue can be linearly related to stress to a reasonable degree of approximation, allowing the use of the equations of linear elasticity as a basis for understanding and modeling dynamic tissue response (16). When these conditions are present, Navier's equation provides two basic ways to convert MR displacement data into elastographic information. First, Eq. [1] can be viewed as a relation for G and λ if \mathbf{u} and ρ are known, so that $\nabla \mathbf{u}$ and $\nabla \cdot \mathbf{u}$ would function as coefficients of the unknowns G and $\lambda + G$, respectively. Rewritten, this can be expressed as the equation

$$\mathcal{F}(G, \lambda) = \nabla \cdot (GA[x, y, z]) + \nabla[(\lambda + G)B[x, y, z]] - \rho C[x, y, z] = 0, \quad [2]$$

where

$$A = \nabla \mathbf{u},$$

$$B = \nabla \cdot \mathbf{u}$$

and

¹Dartmouth College, Thayer School of Engineering, Hanover, New Hampshire.

²Department of Radiology, Dartmouth Hitchcock Medical Center, Lebanon, New Hampshire.

³Norris Cotton Cancer Center, Lebanon, New Hampshire.

Grant sponsor: NIH; Grant number: POI-CA80139.

*Correspondence to: Elijah Van Houten, Ph.D., Dartmouth College, Thayer School of Engineering, HB8000, Hanover, NH 03755.

E-mail: elijah.van.houten@dartmouth.edu

Received 7 June 2000; revised 16 November 2000; accepted 16 November 2000.

$$C = \frac{\partial^2 \mathbf{u}}{\partial t^2}$$

are coefficients derived from the known volumetric MR displacement data, \mathbf{u} . While appealing in its simplicity, this direct inversion method suffers from the required differentiation of the displacement field. In simulation we have found the method to be hypersensitive to noise, leading to significantly degraded elasticity images at very low levels of error in the displacement data, e.g., below 1%. However, certain advanced data conditioning techniques have been shown to reduce this sensitivity (9,11,17,18), making such direct inversion methods more plausible.

Alternatively, MRE reconstructions can be computed through minimization of the squared error between the measured displacements and a set of displacements calculated via Eq. [1] using an assumed elasticity distribution. This initial estimate of the mechanical property distribution is then iteratively updated to improve the match of the calculated displacement field. The basic concept behind this formulation is given elsewhere (13,19–21) and developed in detail for the particular problem of 3D MR elastography in The Inverse Problem (below). As this inversion scheme does not require differentiation of the measured displacement field its susceptibility to imaging noise is minimized, making the method quite robust in the presence of corrupted data (13).

Regardless of the way in which Eq. [1] is incorporated into the inversion process, it is, by nature, a 3D relationship that can only be simplified to two dimensions under special circumstances. It has been found previously (14) that the data-model match between the assumed medium behavior and the true physics of the material in question is critical to the performance of nonlinear optimization-based inversion schemes. It is easy to imagine, therefore, that inaccuracies in the assumption of 2D behavior in the imaging region for MRE could represent a significant compromise in the quality of the reconstructed property image. This article details the development of a subzone-based inversion scheme that takes into account the full 3D nature of Eq. [1]. Examples of the algorithm's capabilities are provided both in comparison with 2D methods for a regular geometry where the presence of symmetry might be anticipated to simplify the dimensionality of the inversion problem and for a complicated, asymmetric, biologically based geometry where no 2D simplification would be expected.

METHODS

Both reconstruction methods described above operate on the solution of the forward problem; that is, the domain behavior generated by the PDE description and the imposed boundary conditions under a known (or assumed) property distribution. In the case of Navier's equation of linear elastic behavior, Eq. [1], the solution of the forward problem provides the displacement conditions everywhere within the domain. The inverse problem, then, is the conversion of this displacement solution into a final property distribution estimate throughout the domain, specifically, the elasticity parameters.

The Forward Problem

To study the impact of 3D effects in the displacement field used for solution of the inverse problem, regular and irregular geometries have been analyzed using the finite element method (FEM). The derivation of the FEM formulation for Eq. [1] is well documented (22) and our particular approach has been described elsewhere for 2D problems (13). In three dimensions the full set of equations implied in Eq. [1] can be written in component form as:

$$\begin{aligned} \hat{\mathbf{x}}: \frac{\partial}{\partial x} G \frac{\partial u}{\partial x} + \frac{\partial}{\partial y} G \frac{\partial u}{\partial y} + \frac{\partial}{\partial z} G \frac{\partial u}{\partial z} + \frac{\partial}{\partial x} \left[(\lambda + G) \left(\frac{\partial u}{\partial x} + \frac{\partial v}{\partial y} + \frac{\partial w}{\partial z} \right) \right] &= \rho \frac{\partial^2 u}{\partial t^2} \\ \hat{\mathbf{y}}: \frac{\partial}{\partial x} G \frac{\partial v}{\partial x} + \frac{\partial}{\partial y} G \frac{\partial v}{\partial y} + \frac{\partial}{\partial z} G \frac{\partial v}{\partial z} + \frac{\partial}{\partial y} \left[(\lambda + G) \left(\frac{\partial u}{\partial x} + \frac{\partial v}{\partial y} + \frac{\partial w}{\partial z} \right) \right] &= \rho \frac{\partial^2 v}{\partial t^2} \\ \hat{\mathbf{z}}: \frac{\partial}{\partial x} G \frac{\partial w}{\partial x} + \frac{\partial}{\partial y} G \frac{\partial w}{\partial y} + \frac{\partial}{\partial z} G \frac{\partial w}{\partial z} + \frac{\partial}{\partial z} \left[(\lambda + G) \left(\frac{\partial u}{\partial x} + \frac{\partial v}{\partial y} + \frac{\partial w}{\partial z} \right) \right] &= \rho \frac{\partial^2 w}{\partial t^2}, \quad [3] \end{aligned}$$

where u , v , and w are the x , y , and z components of the displacement vector \mathbf{u} , respectively. In certain cases, namely, when the out-of-plane stresses or strains are negligible, the above relationships can be simplified to a 2D problem (17). The requirement that the out-of-plane stresses be zero can be written as:

$$\sigma_z = \lambda \left(\frac{\partial u}{\partial x} + \frac{\partial v}{\partial y} + \frac{\partial w}{\partial z} \right) + 2G \frac{\partial w}{\partial z} = 0,$$

$$\sigma_{xz} = G \left(\frac{\partial u}{\partial z} + \frac{\partial w}{\partial x} \right) = 0$$

and

$$\sigma_{yz} = G \left(\frac{\partial v}{\partial z} + \frac{\partial w}{\partial y} \right) = 0, \quad [4]$$

known as the plane stress conditions, while the analogous plane strain relationships can be written as:

$$\epsilon_z = \frac{\partial w}{\partial z} = 0,$$

$$\epsilon_{xz} = \frac{1}{2} \left(\frac{\partial u}{\partial z} + \frac{\partial w}{\partial x} \right) = 0$$

and

$$\epsilon_{yz} = \frac{1}{2} \left(\frac{\partial v}{\partial z} + \frac{\partial w}{\partial y} \right) = 0. \quad [5]$$

The three-dimensional FEM formulation of Eq. [3] is facilitated by the expansion of the approximate displacement solution onto the basis set ϕ , so that:

$$\hat{u} = \sum u_j \phi_j,$$

$$\hat{v} = \sum v_j \phi_j$$

and

$$\hat{w} = \sum w_j \phi_j. \quad [6]$$

Appropriate utilization of divergence and gradient integral theorems then transforms the weighted residual weak form of Eq. [1] into the discrete algebraic system:

$$[\mathbf{A}]\{\hat{\mathbf{u}}\} = \{\mathbf{b}\}, \quad [7]$$

with matrix $[\mathbf{A}]$ having the subelements:

$$[a_{ij}] = \begin{bmatrix} \alpha_{11} & \alpha_{12} & \alpha_{13} \\ \alpha_{21} & \alpha_{22} & \alpha_{23} \\ \alpha_{31} & \alpha_{32} & \alpha_{33} \end{bmatrix}, \quad [8]$$

where

$$\alpha_{11} = \left\langle \frac{\partial \phi_i}{\partial x} (2G + \lambda) \frac{\partial \phi_j}{\partial x} + \frac{\partial \phi_i}{\partial y} G \frac{\partial \phi_j}{\partial y} + \frac{\partial \phi_i}{\partial z} G \frac{\partial \phi_j}{\partial z} - \rho \omega^2 \phi_i \phi_j \right\rangle$$

$$\alpha_{12} = \left\langle \frac{\partial \phi_i}{\partial x} \lambda \frac{\partial \phi_j}{\partial y} + \frac{\partial \phi_i}{\partial y} G \frac{\partial \phi_j}{\partial x} \right\rangle$$

$$\alpha_{13} = \left\langle \frac{\partial \phi_i}{\partial x} \lambda \frac{\partial \phi_j}{\partial z} + \frac{\partial \phi_i}{\partial z} G \frac{\partial \phi_j}{\partial x} \right\rangle$$

$$\alpha_{21} = \left\langle \frac{\partial \phi_i}{\partial y} \lambda \frac{\partial \phi_j}{\partial x} + \frac{\partial \phi_i}{\partial x} G \frac{\partial \phi_j}{\partial y} \right\rangle$$

$$\alpha_{22} = \left\langle \frac{\partial \phi_i}{\partial x} G \frac{\partial \phi_j}{\partial x} + \frac{\partial \phi_i}{\partial y} (2G + \lambda) \frac{\partial \phi_j}{\partial y} + \frac{\partial \phi_i}{\partial z} G \frac{\partial \phi_j}{\partial z} - \rho \omega^2 \phi_i \phi_j \right\rangle$$

$$\alpha_{23} = \left\langle \frac{\partial \phi_i}{\partial y} \lambda \frac{\partial \phi_j}{\partial z} + \frac{\partial \phi_i}{\partial z} G \frac{\partial \phi_j}{\partial y} \right\rangle$$

$$\alpha_{31} = \left\langle \frac{\partial \phi_i}{\partial z} \lambda \frac{\partial \phi_j}{\partial x} + \frac{\partial \phi_i}{\partial x} G \frac{\partial \phi_j}{\partial z} \right\rangle$$

$$\alpha_{32} = \left\langle \frac{\partial \phi_i}{\partial z} \lambda \frac{\partial \phi_j}{\partial y} + \frac{\partial \phi_i}{\partial y} G \frac{\partial \phi_j}{\partial z} \right\rangle$$

$$\alpha_{33} = \left\langle \frac{\partial \phi_i}{\partial x} G \frac{\partial \phi_j}{\partial x} + \frac{\partial \phi_i}{\partial y} G \frac{\partial \phi_j}{\partial y} + \frac{\partial \phi_i}{\partial z} (2G + \lambda) \frac{\partial \phi_j}{\partial z} - \rho \omega^2 \phi_i \phi_j \right\rangle$$

for time-harmonic motion, where $\partial^2 \mathbf{u} / \partial t^2 = -\omega^2 \mathbf{u}$. The vectors of unknown nodal displacements and right-hand-side forcing terms are written as:

$$\{\hat{\mathbf{u}}\} = \{\hat{u}_1, \hat{v}_1, \hat{w}_1, \hat{u}_2, \hat{v}_2, \hat{w}_2, \dots, \hat{u}_N, \hat{v}_N, \hat{w}_N\}^T, \quad [9]$$

and

$$b_i = \begin{bmatrix} \hat{\mathbf{x}} \cdot \left[\oint \mathcal{T} \cdot \hat{\mathbf{n}} \phi_i ds \right] \\ \hat{\mathbf{y}} \cdot \left[\oint \mathcal{T} \cdot \hat{\mathbf{n}} \phi_i ds \right] \\ \hat{\mathbf{z}} \cdot \left[\oint \mathcal{T} \cdot \hat{\mathbf{n}} \phi_i ds \right] \end{bmatrix}, \quad [10]$$

where i and j count from 1 to N , the total number of nodes in the finite element mesh. Here, \mathcal{T} is the conventional stress tensor for linear elasticity (15).

The Inverse Problem

A fully 3D subzone-based inversion algorithm has been developed as a means of avoiding any limitations that may result from the various 2D approximations available through the theory of linear elasticity. As reported for 2D formulations, the subzone approach to the iterative reconstruction scheme allows a high degree of spatial resolution to be maintained while preserving a reasonable computational load (13). This concept readily extends to 3D problems and, in fact, becomes even more important as the computational considerations are far more critical. The 3D subzone process takes advantage of the presence of a full field displacement solution by using the known internal displacements to drive an iterative inversion process of the type shown in Eq. [13] on small partitions of the total problem domain. In this manner, the global inversion process is reduced to multiple local inversion problems:

$$F(E) = \sum F_z(E_z), \quad [11]$$

where

$$F_z(E_z) = \sum_{l=1}^{N_z} (u_l^m - u_l^c)^2 + (v_l^m - v_l^c)^2 + (w_l^m - w_l^c)^2 \quad [12]$$

is the objective function for subzone z to be minimized by the nonlinear iteration process. This function compares the measured displacement data, superscript m , to calculated displacement values, superscript c , and its minimization is carried out by setting its derivatives with respect to Young's modulus, E , to zero and solving the resulting nonlinear system by use of Newton's method. The process can be expressed as a matrix equation:

$$[(\mathbf{H} + \beta \mathbf{I})]\{\Delta \mathbf{E}\} - \{\mathbf{f}\} = \mathbf{0}, \quad [13]$$

where the subzone index z has been dropped and \mathbf{H} is the approximate Hessian matrix, β is a regularization parameter added to facilitate the inversion of \mathbf{H} , $\Delta \mathbf{E}$ is the elastic property update for the current iteration, and \mathbf{f} is the gradient term, $\partial F / \partial E$, containing the current error between the measured and calculated displacements. To implement this formulation discretely, the Young's modulus distribution is described on the same basis set as the dis-

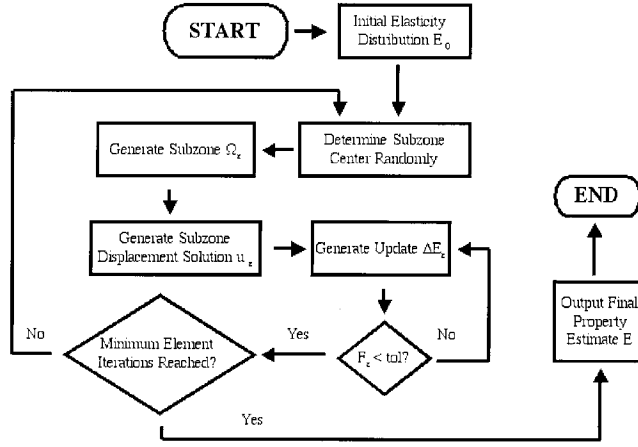


FIG. 1. Flow diagram of the 3D subzone inversion process, where convergence is tested by the size of the minimized subzone functional, F_i , relative to tolerance, tol . Property reconstruction from an initial elasticity distribution takes place on subzones generated in a random order. No global forward solution on the complete problem domain is required by the algorithm.

placement variables, so that $E = \sum_k E_k \phi_k$. The derivative terms, $\partial \mathbf{u} / \partial E_k$, required for solution in this manner can then be generated from the formulation of the discrete forward calculation, Eq. [7], so that:

$$\frac{\partial \hat{\mathbf{u}}}{\partial E_k} = -[\mathbf{A}]^{-1} \frac{\partial \mathbf{A}}{\partial E_k} \cdot \hat{\mathbf{u}}, \quad [14]$$

where $\partial \mathbf{A} / \partial E_k$ has terms $\partial \alpha_{ij} / \partial E_k$, corresponding to α_{ij} in Eq. [9].

$$\frac{\partial \alpha_{11}}{\partial E_k} = \left\langle \frac{\partial \phi_i}{\partial x} \phi_k (2G' + \lambda') \frac{\partial \phi_j}{\partial x} + \frac{\partial \phi_i}{\partial y} \phi_k G' \frac{\partial \phi_j}{\partial y} + \frac{\partial \phi_i}{\partial z} \phi_k G' \frac{\partial \phi_j}{\partial z} \right\rangle$$

$$\frac{\partial \alpha_{12}}{\partial E_k} = \left\langle \frac{\partial \phi_i}{\partial x} \phi_k \lambda' \frac{\partial \phi_j}{\partial y} + \frac{\partial \phi_i}{\partial y} \phi_k G' \frac{\partial \phi_j}{\partial x} \right\rangle$$

$$\frac{\partial \alpha_{13}}{\partial E_k} = \left\langle \frac{\partial \phi_i}{\partial x} \phi_k \lambda' \frac{\partial \phi_j}{\partial z} + \frac{\partial \phi_i}{\partial z} \phi_k G' \frac{\partial \phi_j}{\partial x} \right\rangle$$

$$\frac{\partial \alpha_{21}}{\partial E_k} = \left\langle \frac{\partial \phi_i}{\partial y} \phi_k \lambda' \frac{\partial \phi_j}{\partial x} + \frac{\partial \phi_i}{\partial x} \phi_k G' \frac{\partial \phi_j}{\partial y} \right\rangle$$

$$\frac{\partial \alpha_{22}}{\partial E_k} = \left\langle \frac{\partial \phi_i}{\partial x} \phi_k G' \frac{\partial \phi_j}{\partial x} + \frac{\partial \phi_i}{\partial y} \phi_k (2G' + \lambda') \frac{\partial \phi_j}{\partial y} + \frac{\partial \phi_i}{\partial z} \phi_k G' \frac{\partial \phi_j}{\partial z} \right\rangle$$

$$\frac{\partial \alpha_{23}}{\partial E_k} = \left\langle \frac{\partial \phi_i}{\partial y} \phi_k \lambda' \frac{\partial \phi_j}{\partial z} + \frac{\partial \phi_i}{\partial z} \phi_k G' \frac{\partial \phi_j}{\partial y} \right\rangle$$

$$\frac{\partial \alpha_{31}}{\partial E_k} = \left\langle \frac{\partial \phi_i}{\partial z} \phi_k \lambda' \frac{\partial \phi_j}{\partial x} + \frac{\partial \phi_i}{\partial x} \phi_k G' \frac{\partial \phi_j}{\partial z} \right\rangle$$

$$\frac{\partial \alpha_{32}}{\partial E_k} = \left\langle \frac{\partial \phi_i}{\partial z} \phi_k \lambda' \frac{\partial \phi_j}{\partial y} + \frac{\partial \phi_i}{\partial y} \phi_k G' \frac{\partial \phi_j}{\partial z} \right\rangle$$

$$\frac{\partial \alpha_{33}}{\partial E_k} = \left\langle \frac{\partial \phi_i}{\partial x} \phi_k G' \frac{\partial \phi_j}{\partial x} + \frac{\partial \phi_i}{\partial y} \phi_k G' \frac{\partial \phi_j}{\partial y} + \frac{\partial \phi_i}{\partial z} \phi_k (2G' + \lambda') \frac{\partial \phi_j}{\partial z} \right\rangle,$$

with $G' = \partial G / \partial E_k$, $\lambda' = \partial \lambda / \partial E_k$ and $\partial b / \partial E_k = 0$ as no terms involving E_k appear in the right-hand-side forcing terms since the boundary integrals in Eq. [10] are removed in favor of type I displacement data enforced at the zone boundary.

In the case of a 3D inversion scheme the conservation of computational cost takes on an additional element not essential to the development of an inversion process based on plane stress or plane strain approximations. In the 2D reconstruction algorithm, the processing order of the subzones was determined from global error calculations generated through a full domain forward solution given the latest global property estimate. This type of forward calculation on a highly resolved 3D finite element mesh is a significant computational undertaking. Since the global forward calculation's only role in the 2D reconstruction algorithm was that of a sequence generator for the subzone selection process, it was replaced in the 3D inversion scheme with a significantly more efficient random selection strategy where the center of each subzone is randomly chosen from the centroids of the available elements whose nodal properties have not yet been iteratively updated in the current global subzone sweep. Figure 1 shows a schematic of the algorithmic decision-making for our current 3D version of the subzone approach. Other than the lack of a global solution during the inversion process and the random selection of the subzone processing order, the 3D subzone-based reconstruction algorithm operates in a nearly identical fashion to the 2D process discussed in (13), with spatial filtering being applied both at the subzone level and globally after every node has received at least one reconstruction update.

RESULTS

The FEM formulations shown above are used to investigate both the impact of 3D motion effects on the performance of 2D reconstruction algorithms and the ability of a

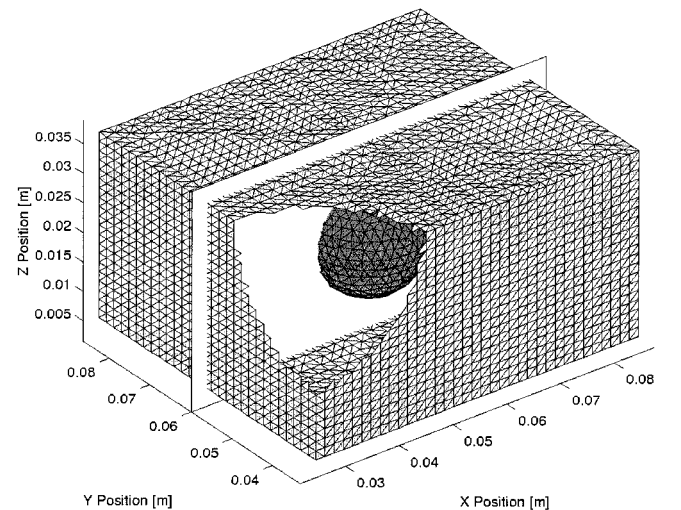


FIG. 2. The outer boundary of the gel phantom box mesh, with the center slice most favorable for 2D motion approximations indicated in white. The centrally located spherical inclusion is visible in gray.

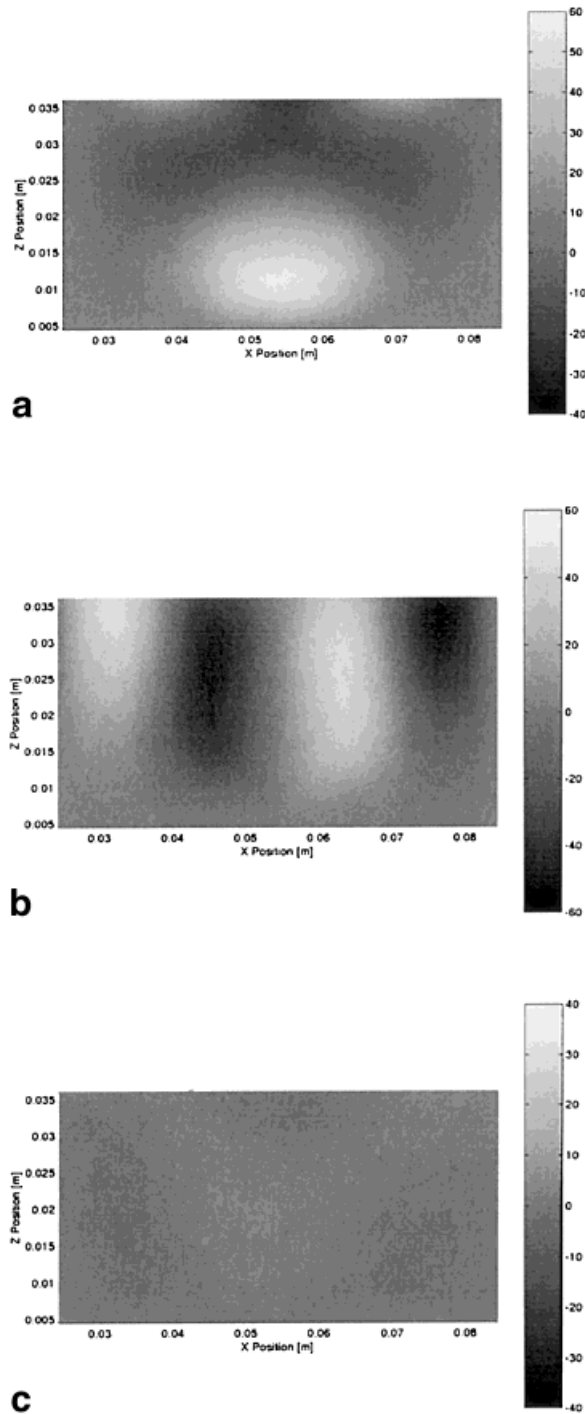


FIG. 3. The displacement solution, in μm , for the gel phantom mesh in the central plane indicated in Fig. 2. The colorbars indicate the range of x-directed displacements, shown in **a**, x: $[-13.466$ to $54.626 \mu\text{m}]$ and the range of z-directed displacements, shown in **b**, z: $[-48.425$ to $46.808 \mu\text{m}]$. The out-of-plane displacements (**c**) in the y-direction.

fully 3D inversion process to deduce mechanical property distributions in regular and irregular 3D geometries.

The Forward Problem

Here we use the 3D forward problem solution to examine the ability of a 2D reconstruction algorithm to invert a

planar displacement solution generated in a 3D body. A 2D reconstruction scheme by definition operates on motion data within a single plane of interest. For such an inversion method to be viable for displacements generated in a 3D geometry, there must exist a plane in which the displacement solution from the 3D body can be approximated to a reasonable extent using the 2D assumptions indicated in Eqs. [4] and [5]. A regular geometry with multiple symmetries might provide a plane in which the 2D and 3D displacement solutions are coherent. To examine this possibility, a regularly shaped mesh was generated using dimensions obtained from an agar gel sample used during phantom studies for the MR displacement imaging process. The phantom is essentially a rectangular gel body with a spherical central inclusion, as shown in the exploded boundary surface image in Fig. 2, with Young's moduli of 60 kPa for the inclusion and 20 kPa for the background gel. A Poisson's ratio of 0.48 was used for the simulated gel phantom. The most eligible plane for accu-

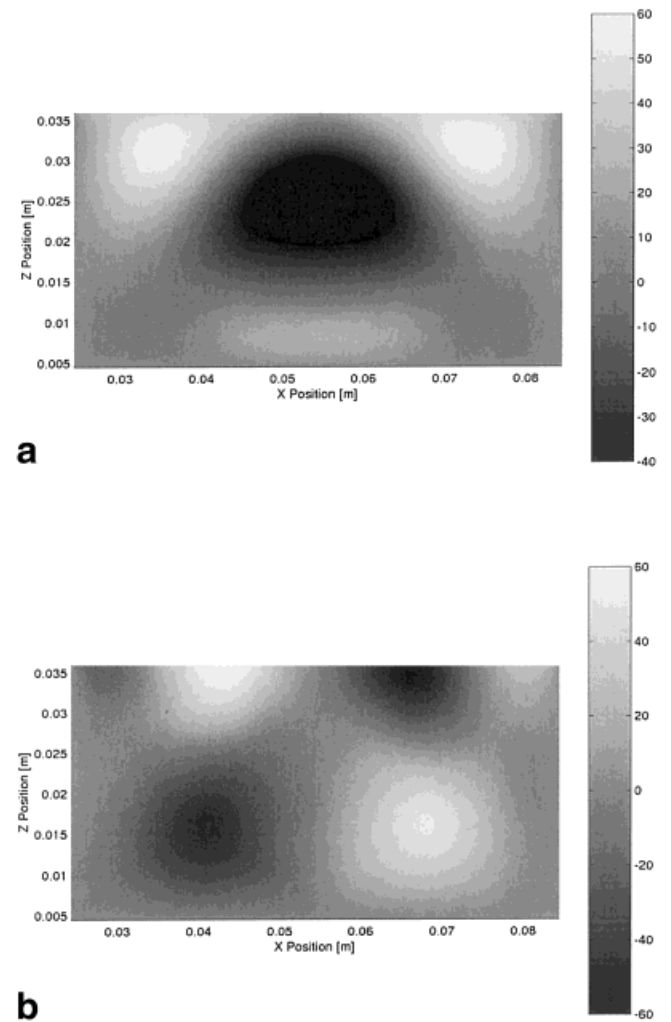


FIG. 4. Same as Fig. 3 for solution using the 2D plane stress approximation. The out-of-plane displacement corresponding to Fig. 3c is not generated in the plane stress approximation. The range of x-directed displacements (**a**) x: $[-56.308$ to $60.481 \mu\text{m}]$ and the range of z-directed displacements (**b**) z: $[-60.480$ to $60.606 \mu\text{m}]$.

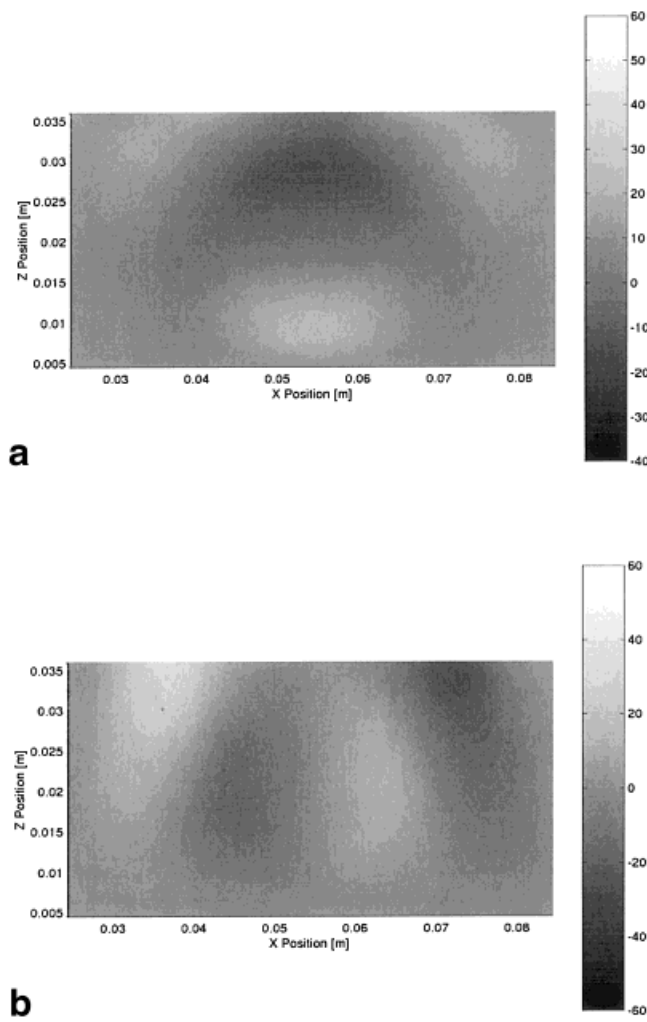


FIG. 5. Same as Fig. 4 for the plane strain approximation. The range of x -directed displacements (a) x : $[-13.651$ to $25.498 \mu\text{m}]$ and the range of z -directed displacements (b) z : $[-30.121$ to $31.224 \mu\text{m}]$.

rate 2D approximations would be the xz plane that passes through the center of the rectangular area, shown in white in Fig. 2. Here, the boundary conditions on either side of the plane are identical, with the only nonsymmetry resulting from differing boundary conditions at the top and bottom of the box, i.e., the upper and lower constant xy planes, respectively. The upper surface of the phantom is free of normal stress, whereas the lower surface is assumed to be perfectly adhered to the surrounding box in which the phantom is contained, having displacement boundary conditions equal to the displacement of the actuating box. This is assumed to be the case for all other sides of the phantom as well, where the actuation was given as 100 Hz

harmonic motion with an amplitude of $10 \mu\text{m}$ in the \hat{x} direction.

The steady-state displacement solutions along the xz plane are shown in Figs. 3a–c, 4a,b, and 5a,b, representing the 3D plane stress and plane strain assumptions, respectively. Although there are certain similarities in these displacement fields, they are not identical. Table 1 indicates the differences between the three solutions by showing their displacement ranges in the xz plane. Further, Fig. 6a,b shows the values of the out-of-plane stress and strain components, calculated from the full 3D displacement solution, which are required to be negligible for the 2D plane approximations to be valid. For this particular box geometry and slice selection, the three stress components that would be required to be zero for the plane stress approximation of Eq. [4] to be valid would be σ_y shown in Fig. 6a, and σ_{xy} and σ_{yz} (not shown). While the σ_{xy} and σ_{yz} components do not differ sizably from zero, significant stresses appear in the σ_y component, indicating a poor match with the plane stress approximation. Similarly, the three strain components required to be close to zero for an accurate plane strain approximation, as in Eq. [5], are ϵ_y , shown in Fig. 6b, and ϵ_{xy} and ϵ_{yz} (not shown). While ϵ_{xy} and ϵ_{yz} are effectively small enough in magnitude for the plane strain approximation to hold, Fig. 6b shows nonnegligible levels of normal strain in the \hat{y} direction, making the plane strain approximation inaccurate.

The Inverse Problem

The ultimate test of the fidelity of plane stress and plane strain approximations for inverting a simple 3D phantom displacement field is demonstrated in Fig. 7, which shows the results of the 2D, subzone-based inversion scheme detailed in (13) operating on the x and z components of the 3D displacement data for the xz plane discussed above. Figure 7a depicts the actual elasticity distribution of this central plane as used for the fully 3D forward calculation. Figure 7b,c shows inversions based on plane stress and plane strain approximations, respectively, of the 3D gel phantom forward problem data with zero added noise. While the presence of a circular stiff inclusion is discernible at the center of the images, the poor quality of the reconstructions is obvious. This indicates that the full 3D displacement field's lack of adherence to either the plane stress or plane strain approximation, as indicated in Fig. 6, is catastrophic in terms of the quality of the inversion solution shown here when compared to the character of the results observed from reconstructions of truly 2D motion fields (13).

Figure 8a,b shows the results, in units of kPa, of the 3D reconstruction algorithm operating on the full volume displacement information, with 15% added noise, for the gel

Table 1
Comparison of 3D and 2D Plane Stress and Plane Strain Displacement Ranges

Sol. type	Max. negative \hat{x} disp.	Max. positive \hat{x} disp.	Max. negative \hat{z} disp.	Max. positive \hat{z} disp.
3D	$-13.466 \mu\text{m}$	$54.626 \mu\text{m}$	$-48.425 \mu\text{m}$	$46.808 \mu\text{m}$
2D plane stress	$-56.308 \mu\text{m}$	$60.481 \mu\text{m}$	$-60.480 \mu\text{m}$	$60.606 \mu\text{m}$
2D plane strain	$-13.651 \mu\text{m}$	$25.498 \mu\text{m}$	$-30.121 \mu\text{m}$	$31.224 \mu\text{m}$

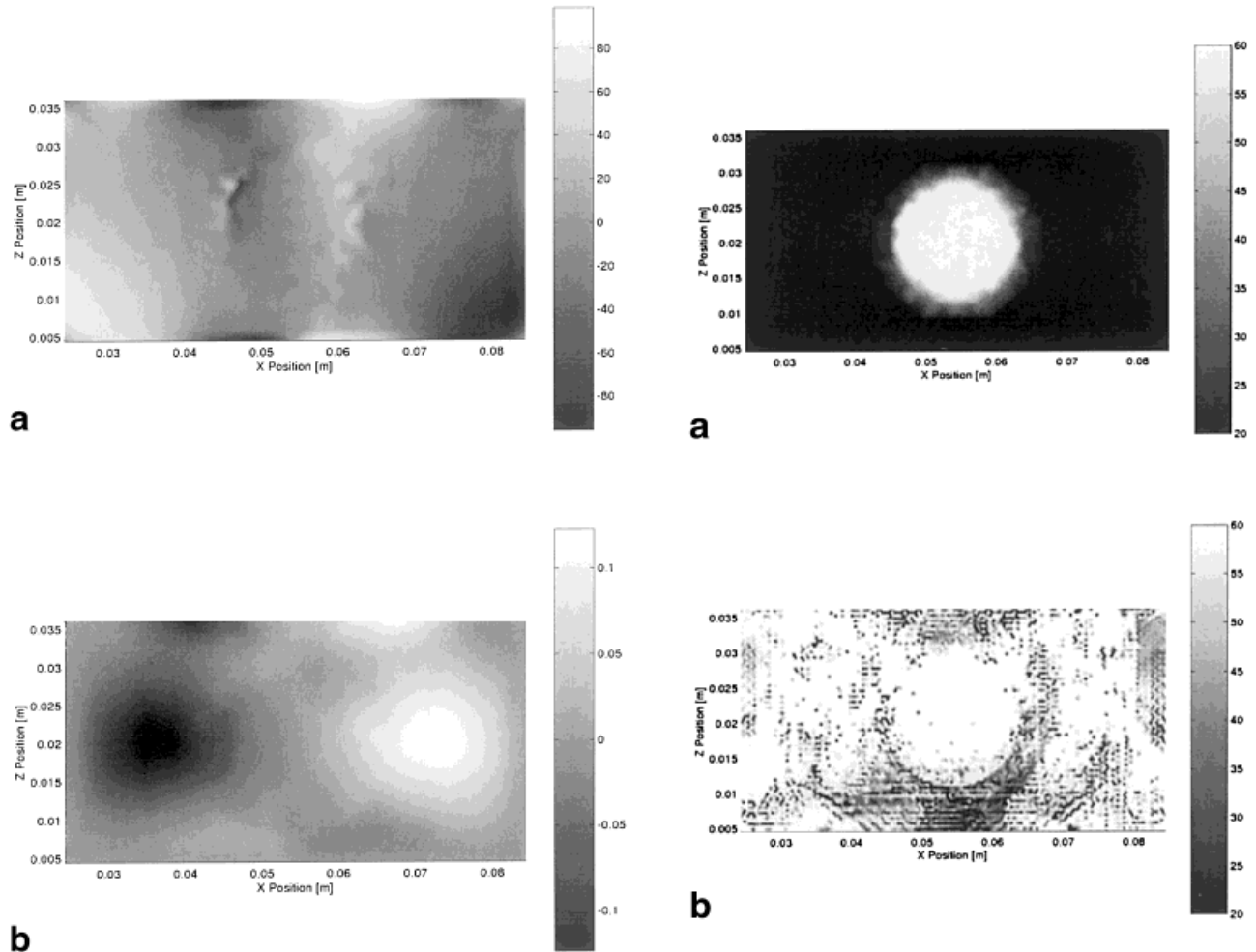


FIG. 6. The stress and strain values, in Pa and percent strain respectively, along the central plane of the gel phantom mesh calculated from the full 3D displacement set. Values of the normal stress component (a), σ_y , are seen to differ from zero by up to 100 Pa in magnitude. Similarly, normal strain (b), ϵ_y , is seen to differ from zero by up to 0.2% strain. Values of the shear stress and strain components, σ_{xy} , σ_{yz} , ϵ_{xy} , and ϵ_{yz} , are negligible and not shown.

box phantom indicated in Fig. 2. Figure 8a presents the solution from a homogeneous initial guess of 60 kPa and an average subzone radius of roughly 5 mm, while Fig. 8b depicts a solution based on the exact same starting distribution but an average subzone radius of nearly 9 mm. Clearly, the images seen in Fig. 8 are superior to those shown in Fig. 7, with the size of the inclusion and its material property value identified in the presence of noisy data. Improvements resulting from changes in the subzone radius are also evident, indicating that the quality of the inversion solution is sensitive to this parameter. Further study and optimization of this sensitivity is needed.

To examine the ability of the 3D inversion algorithm to process displacement fields similar to those that would occur in realistic geometries with irregular property distributions, a finite element mesh has been generated from a breast MR image volume, Fig. 9, with the elastic property distribution obtained by thresholded, scaled, conversion of the MR image intensity values. It is important to note

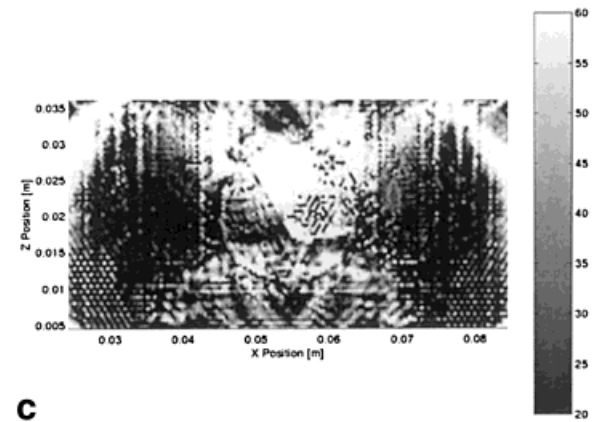


FIG. 7. The original Young's modulus distribution (a), in kPa, used to generate the forward displacement calculation, along the central plane of the gel phantom mesh. Reconstructions of Young's modulus distributions (b,c), again in kPa, based on the two different 2D plane approximations. The plane stress-based inversion of the in-plane displacements (b,c), with no noise added, from the full 3D displacement set along the central plane of the gel phantom mesh. The inclusion is barely visible amid the artifact derived from the inaccuracy of the 2D motion assumption. A similar reconstruction (c) based on the plane strain approximation. Again, the inclusion is noticeable but not clearly indicated.

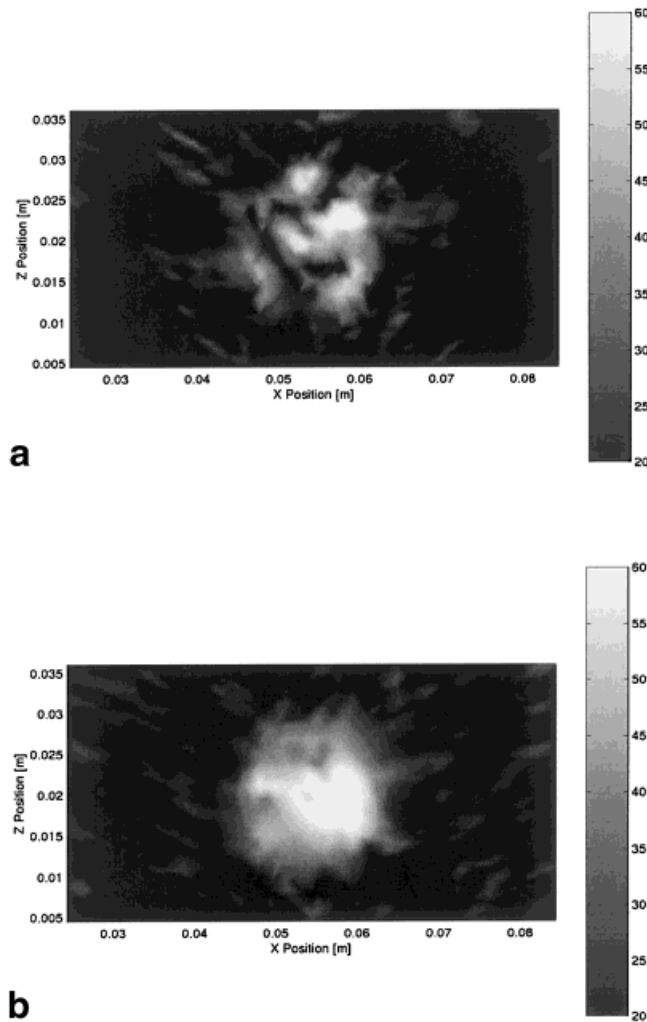


FIG. 8. Two images showing the central plane of reconstructed Young's modulus solutions from the 3D subzone-based inversion algorithm using displacement data corrupted with 15% random noise. A solution (a) where the average subzone radius was roughly 5 mm, containing on average around 180 nodes. A similar solution (b), generated from an identical initial guess of a uniform distribution at 60 kPa, but for a larger subzone size, roughly 8 mm radius on average with around 530 nodes per subzone. The presence of the stiff inclusion is clearly noted, with the solution based on larger subzones demonstrating an improvement over the smaller subzone reconstruction.

here that this method of property distribution generation is used only as an illustration to obtain complicated material property structure for simulation purposes. It is not expected that the mechanical properties of breast tissue will be directly related to standard MR intensity values per se. A steady-state displacement solution in the vertical slice highlighted in Fig. 9b is shown in Fig. 10a–c, indicating x , y , and z directed motion, respectively. Ten μm , 100 Hz excitation was induced at two separate locations along the boundary, centered at points near the chest wall and close to the vertical plane shown in Fig. 9b. As can be seen, this displacement field is highly irregular, with little or no prospect of a plane suitable for 2D motion approximation being found. The full 3D subzone-based inversion algo-

rithm is capable of operating on such complex motion fields, however. Figures 11–13 illustrate some results from reconstructions performed on displacement solutions similar to the one partially described in Fig. 10 after 15% random noise was added to the motion values. Figure 11a shows a material property distribution of the breast mesh with a 5 mm diameter inclusion of 120 kPa Young's modulus, less than two times stiffer than the mean background stiffness, located against the chest wall. A Poisson's ratio of 0.45 was used to approximate biological tissue's nearly incompressible nature. The cross-section presented in this figure corresponds to the vertical slice of Fig. 9b. The reconstructed property distribution is shown in Fig. 11b, where recovery of the inclusion size, location, and stiff-

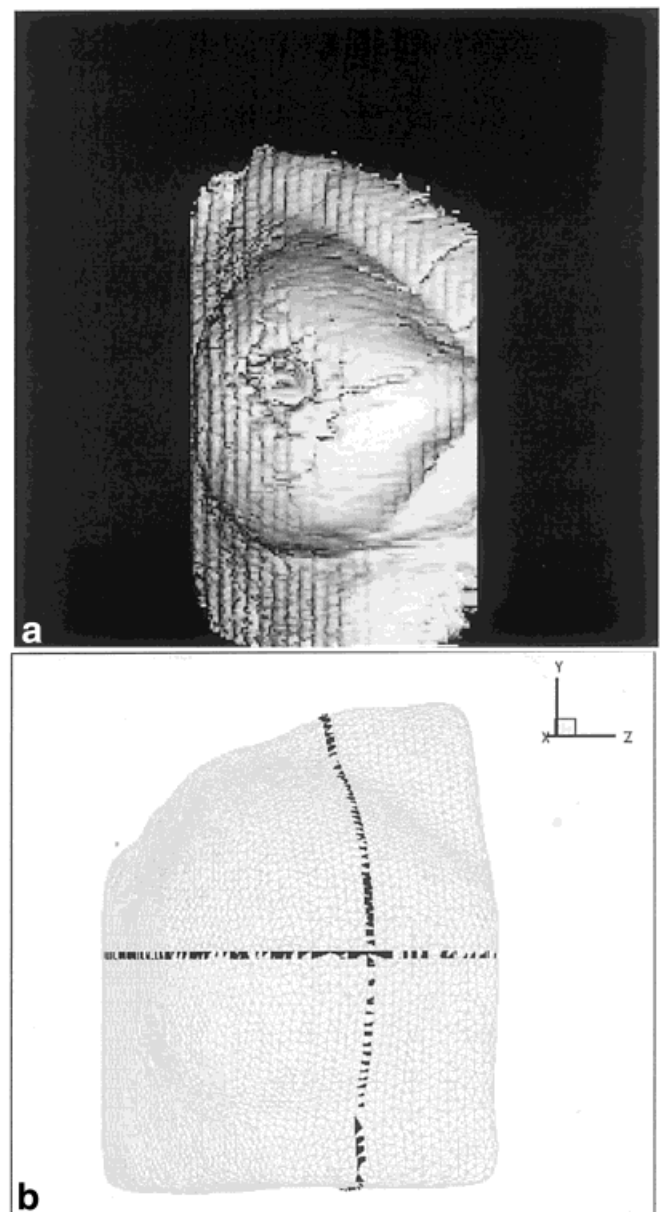


FIG. 9. The 3D breast mesh geometry was developed from an actual patient MR scan (a). The boundary surface (b) of the breast mesh, with the two planes depicted in the following figures indicated in black.

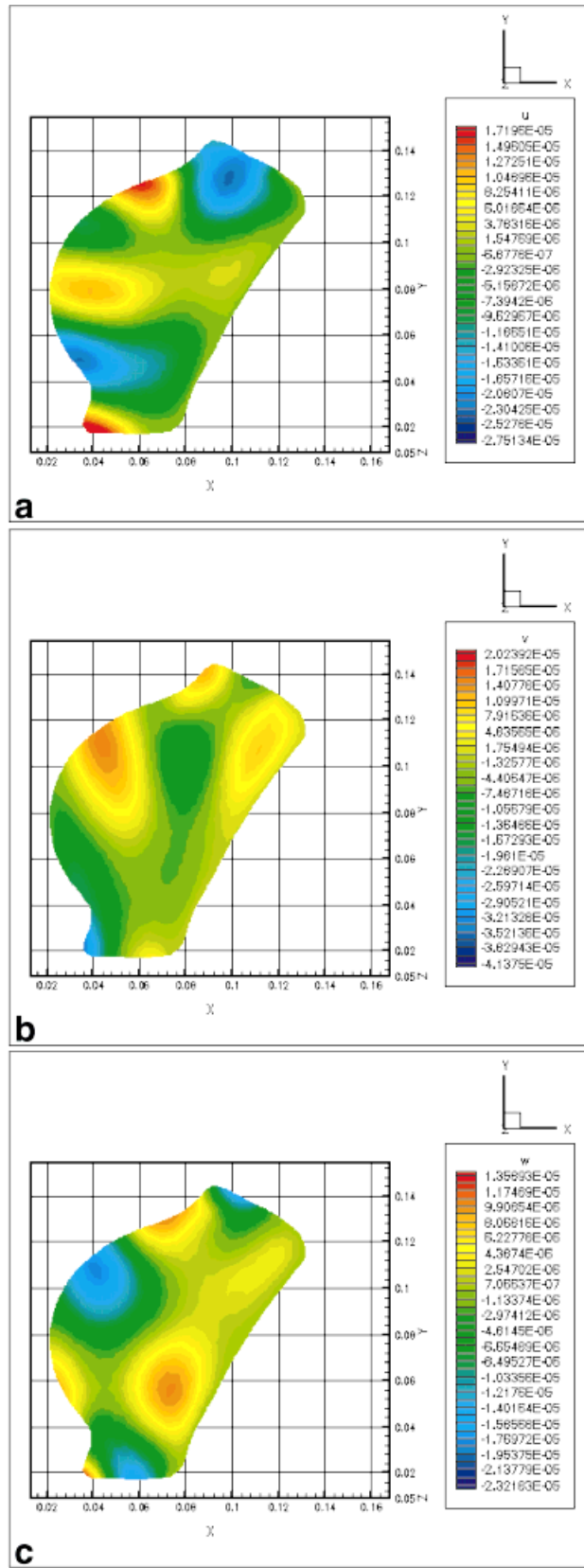


FIG. 10. The 3D displacement solution, in m , along the vertical plane shown in Fig. 9b. **a** contains x -directed displacements, while **b** and **c** show the y - and z -directed motion, respectively.

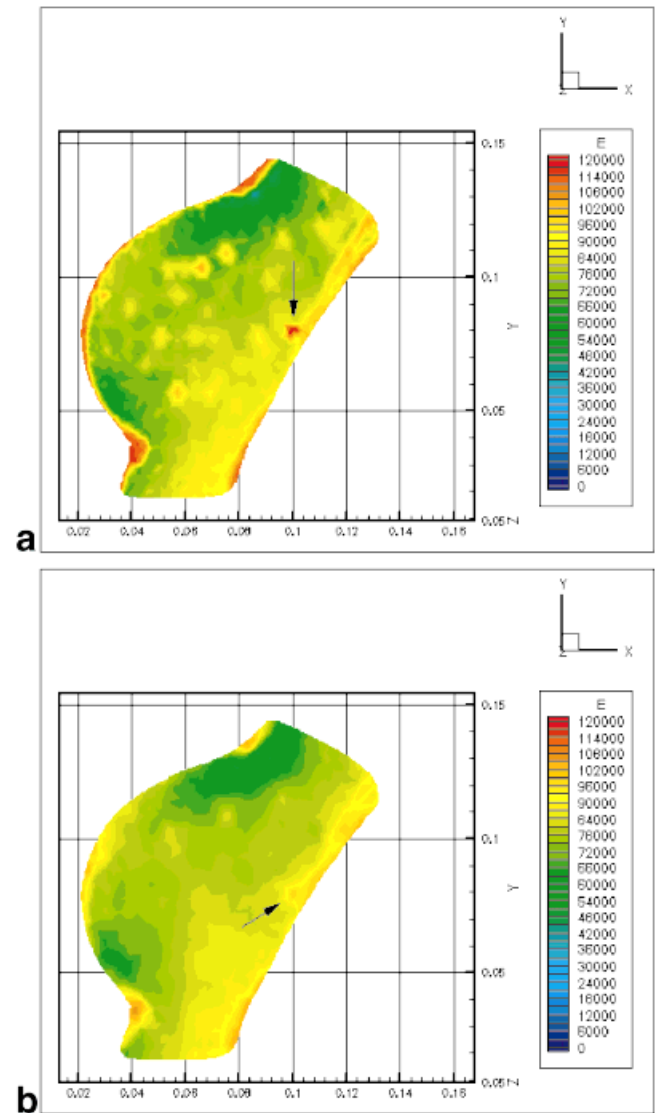


FIG. 11. The original Young's modulus distribution (**a**) along the vertical plane from Fig. 9b in Pa, while **b** shows the reconstruction along this plane from the 3D inversion algorithm based on displacement data with 15% added noise. The location, size, and stiffness of the 5 mm diameter, 120 kPa inclusion along the chest wall are seen to be accurately characterized by the reconstruction algorithm.

ness is seen. Figures 12 and 13 contain similar results for the case of centrally located tumors of 1 cm diameter with moduli of 100 kPa and 200 kPa, respectively.

The slices shown are the horizontal and vertical planes outlined in Fig. 9b. The displacement dataset used for the reconstruction provided in Fig. 13 is the same as that partially illustrated in Fig. 10, while the motion data for Figs. 11–12 are not depicted. The algorithm is able to reconstruct the general property distribution of the heterogeneous mesh and the inclusions indicated are detected, although the exact value of their moduli are not recovered in this case. The inversion algorithm has been found to be sensitive to various parameters such as subzone size (both in terms of number of nodes and actual radius) and the amount of spatial filtering used during solution. Further

study for parametric optimization is needed to determine the full capability of the algorithm.

CONCLUSIONS

Even in highly regular and symmetric geometries, the displacement field of an oscillating, 3D, isotropic, linear elastic body is not accurately characterized through the classic 2D plane approximations commonly used in linear elasticity. Reconstructions of the 3D displacement data based on these 2D plane approximations suffer accordingly. In order to overcome these limitations of a material property reconstruction algorithm based on 2D plane stress or plane strain approximations, a fully 3D elasticity inversion algorithm has been developed. This 3D subzone-based inver-

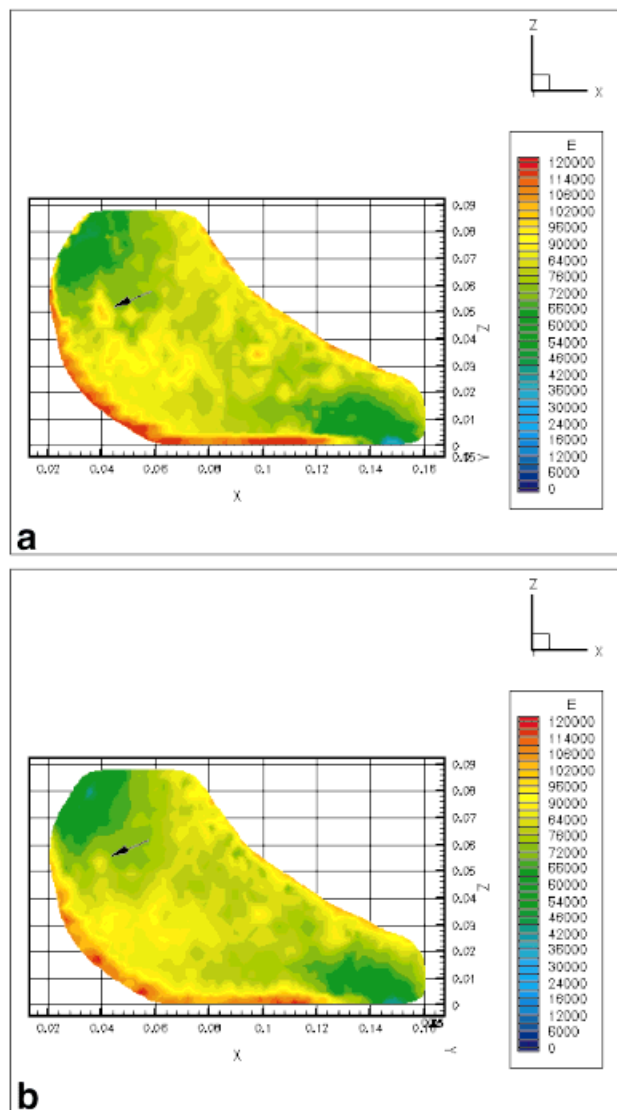


FIG. 12. Young's modulus distribution for the forward problem solution (a) and the reconstructed values (b) from data with 15% added noise, in Pa. The cross-section of the 3D reconstruction solution shown is the horizontal plane indicated in Fig. 9b. The presence of the 1 cm diameter inclusion with a Young's modulus of 100 kPa is indicated in the reconstruction.

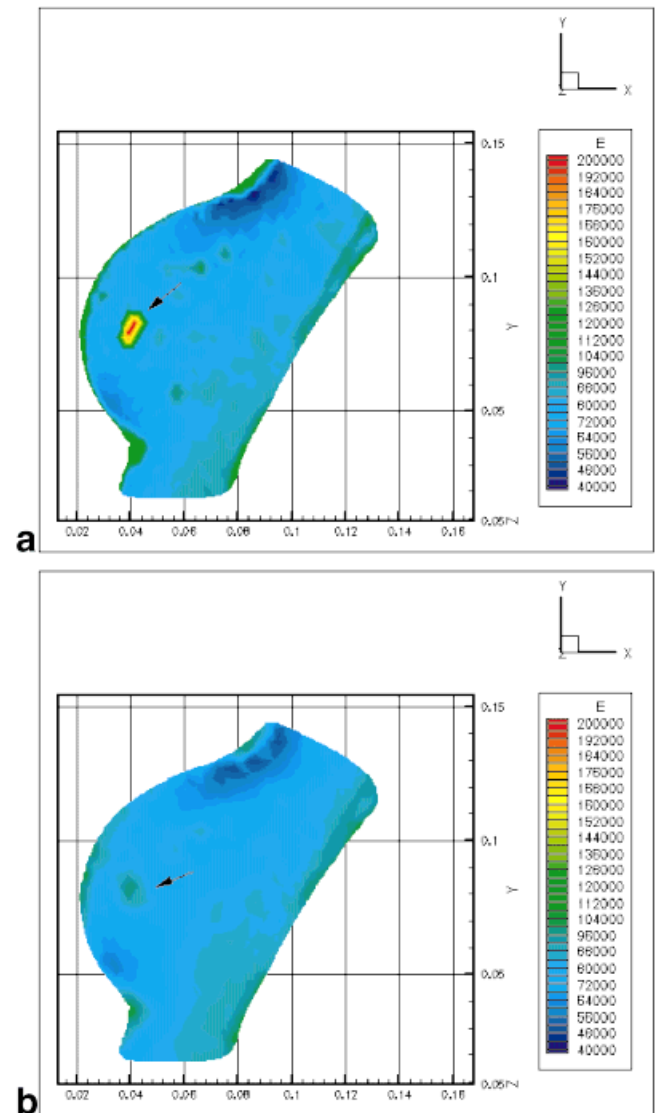


FIG. 13. Reconstruction from the vertical plane of Fig. 9b with the original property distribution (a) and the corresponding plane (b) of the 3D inversion solution from displacement data with 15% added noise, both in Pa. The 1 cm diameter inclusion with a modulus of 200 kPa is detected by the reconstruction algorithm, although the process is not able to accurately estimate the inclusion's stiffness.

sion scheme is shown to reconstruct with reasonable accuracy the Young's modulus distribution in regular 3D objects as well as in highly irregular, biologically based geometries and property distributions, even in the presence of 15% random noise. As in vivo tissue geometries and stiffness distributions promise to be irregular, and therefore poorly characterized by any 2D plane approximation, such fully 3D inversion algorithms are necessary for accurate conversion of in vivo MR displacement data into reliable elastic property information.

REFERENCES

1. Bishop J, Poole G, Leitch M, Plewes DB. Magnetic resonance imaging of shear wave propagation in excised tissue. *J Magn Reson Imag* 1998;8: 1257-1265.

2. Chenevert TL, Emelianov SY, Skovoroda AR. Elasticity reconstructive imaging using static displacement and strain estimations. In: Proc 5th Annual Meeting ISMRM, Vancouver, Canada, 1997.
3. Chenevert TL, Skovoroda AR, O'Donnell M, Emelianov SY. Elasticity reconstruction imaging via stimulated echo MRI. *Magn Reson Med* 1998;39:482–490.
4. Lewa CJ. Magnetic resonance imaging in the presence of mechanical waves. *Spectrosc Lett* 1991;24:55–67.
5. Manduca A, Muthupillai R, Rossman PJ, Greenleaf JF, Ehman RL. Image processing for magnetic resonance elastography. *SPIE* 1996; 2710:616–623.
6. Manduca A, Dutt V, Borup DT, Muthupillai R, Ehman RL, Greenleaf JF. Reconstruction of elasticity and attenuation maps in shear wave imaging: an inverse approach. *Lecture Notes in Computer Science: Medical Image Computing and Computer-Assisted Intervention MICCAI'98*, 1998;1496:606–613.
7. Muthupillai R, Rossman PJ, Lomas DJ, Greenleaf JF, Riederer SJ, Ehman RL. Magnetic resonance elastography by direct visualization of propagating acoustic strain waves. *Science* 1995;269:1854–1857.
8. Muthupillai R, Rossman PJ, Lomas DJ, Greenleaf JF, Riederer SJ, Ehman RL. Magnetic resonance imaging of transverse acoustic strain waves. *Magn Reson Med* 1996;36:266–274.
9. Oliphant TE, Manduca A, Greenleaf JF, Ehman RL. Direct, fast estimation of complex-valued stiffness for magnetic resonance elastography. In: Proc 8th Annual Meeting ISMRM, Denver, 2000. p 540.
10. Plewes DB, Bishop J, Samani A, Sciarretta J. Visualization and quantification of breast cancer biomechanical properties with magnetic resonance elastography. *Phys Med Biol* 2000;45:1591–1610.
11. Sinkus R, Lorenzen J, Schrader D, Lorenzen M, Dargatz M, Holz D. High-resolution tensor MR elastography for breast tumor detection. *Phys Med Biol* 2000;45:1649–1664.
12. Steele DD, Chenevert TL, Skovoroda AR, Emelianov SY. Three-dimensional static displacement, stimulated echo NMR elasticity imaging. *Phys Med Biol* 2000;45:1633–1648.
13. Van Houten EEW, Paulsen KD, Miga MI, Kennedy FE, Weaver JB. An overlapping sub zone technique for MR based elastic property reconstruction. *Magn Reson Med* 1999;42:779–786.
14. Van Houten EEW, Weaver JB, Miga MI, Kennedy FE, Paulsen KD. Elasticity reconstruction from experimental MR displacement data: initial experience with an overlapping subzone finite element inversion process. *Med Phys* 2000;27:101–107.
15. Chou PC, Pagano NJ. Elasticity: tensor, dyadic and engineering approaches. New York: Dover; 1967.
16. Fung YC. Biomechanics: mechanical properties of living tissues, 2nd ed. New York: Springer-Verlag; 1993.
17. Bishop J, Samani A, Sciarretta J, Plewes DB. Use of constraints to produce plane strain conditions for MR elastography. In: Proc 8th Annual Meeting ISMRM, Denver, 2000. p 1735.
18. Skovoroda AR, Lubinski MA, Emelianov SY, Sarvazyan AP, O'Donnell M. Reconstructive elasticity imaging for large deformations. *IEEE Transact Ultrason Ferroelectr Freq Control* 1999;46:523–535.
19. Kallel F, Bertrand M. Tissue elasticity reconstruction using linear perturbation method. *IEEE Trans Med Imag* 1996;15:299–313.
20. Paulsen KD, Jiang H. Spatially varying optical property reconstruction using a finite element diffusing equation approximation. *Med Phys* 1995;22:691–701.
21. Paulsen KD, Jiang H. An enhanced electrical impedance imaging algorithm for hyperthermia applications. *Int J Hypertherm* 1997;13:459–480.
22. Bathe KJ, Wilson EL. Numerical methods in finite element analysis. Englewood Cliffs, NJ: Prentice-Hall; 1967.